Structural glass beams with embedded GFRP, CFRP or steel reinforcement rods
Comparative experimental, analytical and numerical investigations

Bedon, Chiara; Louter, Christian

Important note
To cite this publication, please use the final published version (if applicable).
Please check the document version above.

Structural glass beams with embedded GFRP, CFRP or steel reinforcement rods: Comparative experimental, analytical and numerical investigations

Chiara Bedon[a,*], Christian Louter[b]

[a] University of Trieste, Italy
[b] Delft University of Technology, the Netherlands

A B S T R A C T

The use of hybrid and composite solutions for structural applications represents a common approach for the development of safe design principles. Consolidated examples exist for concrete, steel and masonry structures. As a general rule, materials are combined so as to obtain an enhanced redundancy, strength and/or (lateral) stiffness for these systems. In this paper, structural laminated glass (LG) beams including reinforcement rods are investigated, and special attention is spent on the effect of embedded rod features, consisting of GFRP, CFRP or stainless steel reinforcement tendons. The examined embedded solution, as shown, can offer a certain benefit to the bending performance of traditional LG beams, including positive effects on stiffness, resistance and redundancy. The intrinsic properties of rods can otherwise largely affect the overall observations. To this aim, unpublished experimental tests are first briefly summarised for a set of 1 m span LG beams. Support for the preliminary discussion of the examined design concept is also derived from simple analytical calculations. Finite-Element (FE) numerical simulations are then presented, reporting on major expected behaviours due to variations in the geometrical/mechanical features of the rods, with respect to the experiments. A key role in the FE models is given by the reliable description of mechanical properties and interactions between the structural components. Comparative results are hence discussed for the post-fracture assessment of beam specimens. As shown, even a limited presence of reinforcing rods ($\approx$ 100-to-400 the explored range for the ratio of glass-to-rods cross-sectional area) can provide ductility and redundancy to the LG beams. Maximum benefits (+ 30% residual resistance) are given by ductile steel rods, while positive effects can also be achieved with GFRP and CFRP tendon rods.

1. Introduction

In contemporary architecture, the use of glass as a structural material is ever increasing, especially in facades, where dedicated design methods are required to assess multiple performance aspects. Most of the research studies of literature on glass floors and curtains are focused on thermal and energy performance issues (see for example [1–6], etc.).

Structurally speaking, however, these glass assemblies must offer appropriate load-bearing performances, especially when extreme design loads can be expected (i.e [7].). There, large glass panels can be restrained by glazed beams and fins, with a minimum of metal components. The brittleness of glass, consequently, calls for specific attention to ensure their safety performance, in case of fracture [8,9].

For structural glass beams, in particular, safety concepts have been developed over the past years, making use of reinforcement tendons adhesively bonded at the edge of a given glass cross-section. The basic concept is similar to reinforced concrete, and has been addressed by several research projects (see for example [10]). An extended overview of literature efforts is provided in [11], while more recent advances are presented in [12–14]. Both the design concepts of reinforced and post-tensioned glass beams have demonstrated their feasibility in several research and engineering projects.

More in detail, given a reinforced glass beam in bending, the reinforcement tendons have a key role in case of glass fracture, because they are aimed to bridge cracks in the glass components, while carrying on tensile forces. Together with a compression force in the (un-cracked) compression zone of the so assembled beam, the fractured glass section will hence be able to offer a certain residual resistance and ductility. By pre-tensioning the reinforcement rods, an even more efficient reinforcement system could be obtained, by further increasing the initial fracture strength of glass, and by enhancing its post-cracked performance. On the other hand, the input design parameters should be

---

Fig. 1. Example of double LG beams with embedded GFRP rods [15].

properly defined and assessed, so as to avoid the occurrence of possible undesired effects, such as buckling phenomena (see also Section 4.2).

The current paper extends the studies of literature and focuses on a specific configuration of reinforced glass beams. Rather than bonding the reinforcement at the edge of the glass, in particular, the reinforcement rods are embedded in the polymer interlayer, between the individual glass plies of a laminated glass (LG) section (Fig. 1). Preliminary explorations into such a design concept, see [15–17], have shown the feasibility and potential of embedded Glass Fibre Reinforced Polymer (GFRP) rods for traditional LG beams, but further studies are still required. In [17], in particular, an extended finite element (FE) analysis was validated towards bending test results and carried out to explore the effects of GFRP rods' features (size, type, number, position, including pre-stress) on the actual bending performance of a given glass section (1.5 m the beam span, 115 mm the section height, 8 mm the nominal thickness of each glass layer). The current study adds to those investigations and compares (via unpublished laboratory experiments, analytical models and FE numerical analyses carried out in accordance with [17]) the bending performance of LG beam specimens with three different reinforcement layouts. The reference double LG specimen, in doing so, consists of 1 m long, 10 × 100 mm glass layers. Special care is spent for material properties of rods (namely consisting of GFRP, CFRP or stainless steel rods).

As shown, the general design concept aims to take advantage of the embedded rods, being expected to act as reinforcement tendons and to beneficially interact with the adjacent glass panels, through the polymer foils. As far as minor modifications are considered for the embedded rods, however, a certain sensitivity of the observed structural performances is emphasised, being strictly related to the intrinsic features of the embedded rods, hence resulting in mostly different overall in-plane bending responses, especially in terms of post-fracture resistance, ductility and collapse mechanism. Further sensitivity of the structural observations can then implicitly derive from the glass-to-rods ratio of resisting cross-sections. In this regard, the original bending experiments are first described for 1 m long reinforced LG beams, giving evidence of the global effects due to the embedded rods, as well as of the observed collapse mechanisms. Double LG sections are taken into account for comparative purposes, based on similarities with past research studies and availability of materials. It is worth mentioning, in this regard, that real LG sections for design applications are generally composed, for safety purposes, of a minimum three layers of tempered/heat strengthened glass, being characterised by significantly higher tensile resistances, compared to annealed glass sections herein presented (see for example [9]). Accordingly, the effect and potential of the embedded rods should be further explored, by accounting for different aspect ratios, dimensions, LG beam compositions, etc. After the preliminary discussion of these bending experiments, simplified analytical calculations carried out in accordance with [10] are reported in

the paper, for a first assessment of the test results. Due to the basic assumptions of the past analytical formulation, as shown, rough comparisons can be only carried out, for the geometrical and mechanical features object of analysis. In any case, a certain correlation with the full-scale experiments can be observed, hence the collected results could be used for preliminary design considerations. The major advantage for the interpretation of the experimental observations is indeed derived from FE numerical models, implemented in ABAQUS [18] with the aim to investigate more in detail the actual structural performance of the examined structural typology. As shown, post-fracture comparative calculations can be derived from reliable material models and mechanical interactions between the LG beam components.

2. Reference beam specimens and experimental methods

The investigation summarised in this paper follows and extends the experimental studies briefly reported in [19] (technical report for internal use only), and is aimed to assess more in detail the structural performance of LG beams under quasi-static, monotonic, four-point bending loads, at ambient temperature. To this aim, three beam types (and three specimens per beam type) were tested.

The reference specimen, see Fig. 2(a), was intended as a glass beam prototype, aimed at emphasising the effects of a certain amount of embedded rods, with respect to the resisting section of a traditional, double LG section. As such, for research purposes, each sample consisted of a two-ply LG assembly, with 10 mm × 100 mm the nominal cross-sectional dimensions of each annealed (AN) glass plate, and a SentryGlas® (SG) interlayer to bond them (1.52 mm its nominal thickness). The latter, was chosen - in type and thickness – due to analogy with earlier research studies (see for example [15–17], etc.), as well as based on the availability of materials for the experimental investigation. The nominal length of each beam specimens was then set to 1 m, with setup boundaries and loads according to Fig. 2(b). In doing so, a universal testing machine was used (Zwick 500 kN). Fig. 2(b) shows the bespoke steel support frame in use, so as to provide both lateral and vertical restraints to the LG specimens (see also Figs. 6 and 7 for the physical setup).

Regarding the lateral supports, the steel frame was used to prevent possible out-of-plane displacements of the specimens, and hence to avoid possible lateral-torsional buckling phenomena, so as to ensure a global behaviour of beams in bending with point lateral restraints and limited buckling length (see [20–22]).

At the time of the experiments, in addition, small aluminium plates were interposed between each glass beams and the supports (200 × 30 mm the base dimensions, with 5 mm their thickness), to prevent local stress concentrations due to possible irregularities and misalignments of the specimens in the region of the end supports. Such an assumption, of common use for similar test setup configurations, was considered to do not affect the actual restraint configuration for the tested sample, hence to have negligible effects on the collected measurements (see also Section 4).

Given the key role that tendon rods can have on the overall performance of traditional LG systems, especially in their post-fracture behaviour, most of attention of the experimental study herein discussed was spent for the effects due to various features for the rods in use (see Fig. 2(a)). Variations in the specimens' series, more in detail, included modifications of the type and cross-sectional size of the embedded rods, hence resulting in LG beams with three round rods composed of:

- GFRP (φ = 2 mm their nominal diameter),
- CFRP (φ = 1.5 mm),
- stainless steel (AISI 304 type, with φ = 3 mm),

and being embedded within the middle SG foils, in accordance with Fig. 2(b).

Geometrical and mechanical features of interest for the rods in use,
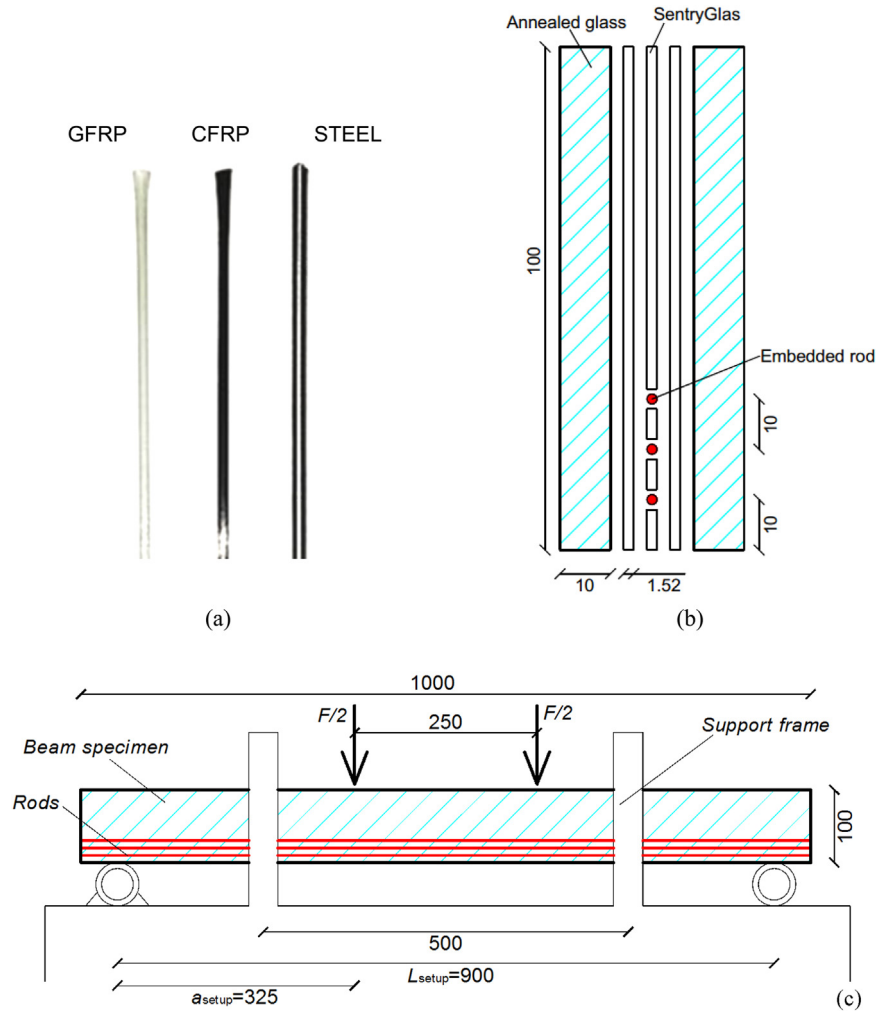
Fig. 2. (a) GFRP, CFRP and steel rods in use, with (b) nominal cross-section (exploded view) of the reference beam specimen [15], and (c) test setup (front view). All the dimensions are given in mm.

Table 1
Nominal geometrical and mechanical properties of rods in use for the experimental tests, in accordance with producer datasheets and design standards [27–29].

			GFRP	CFRP	STEEL
Rod diameter	[mm]	ϕ	2	1.5	3
Rod area	[mm^2]	A_{rod}	3.14	1.77	7.07
Number of rods	–	n_{rod}	3	3	3
Total area	[mm^2]	$A_{rod,tot}$	9.42	5.30	21.21
Glass-to-rods A-ratio	–	R_A	≈ 212	≈ 377	≈ 94
Volume fraction	[%]	v_{rod}	63	60	n.a.
Fibre filaments type	–	–	E-glass	S-glass	n.a.
Tensile strength	[MPa]		$f_{rod,y} = f_{rod,u} = 3400^*$	$f_{rod,y} = f_{rod,u} = 2500^*$	$f_{rod,y} = 260$
			$f_{rod,y} = f_{rod,u} = 1607^{**}$	$f_{rod,y} = f_{rod,u} = 1500^{**}$	$f_{rod,u} = 850$
Elongation at rupture	[%]	$\varepsilon_{rod,u}$	3.6	1.5	10
Modulus of elasticity	[GPa]	E_{rod}	40	140	210
Elastic bending stiffness EI-ratio	–	R_{EI}	1.005	1.002	1.030
Density	[kg/m^3]	ρ_{rod}	2600	1770	7850
Rods weight	[kg]	W_{rod}	0.025	0.009	0.166
W-ratio	–	R_W	1.005	1.005	1.033

Key: * = virgin value; ** = effective value (in use for calculations); n.a. = not available y = yielding; u = ultimate value at rupture.

and the so assembled beam specimens, are summarised in Table 1. In the table, given the reference mechanical features of AN glass and SG foils (see [3,24–26]), the key nominal properties of the reinforcements in use are reported, as derived from technical data sheets of producers and/or design product standards [27–29].

All the experiments were carried out at ambient conditions (23 °C the average temperature), with 1 mm/min the displacement rate up to

initial fracture, and 5 mm/min the imposed displacement rate for the remainder of each test. The so defined displacement rates were selected in accordance with earlier investigations ([15], etc.), for comparative purposes, and were kept equal for the full set of specimens.

Globally, the total duration of each experiment was in the order of 30–45 min. In such a time interval, the vertical displacement at the mid-span section of each specimens was continuously monitored, both in the

form of testing machine displacement measurements and LG beams deformations, via a set of linear transducers. Given such a double measurement of deflections, however, the post-processing phase of all the test results summarised in Section 5.1 generally emphasised - especially in terms of post-fracture stage, being of primary interest for the current research study - mostly coincident machine/transducer measurements for the examined specimens (2% their average scatter).

Worth of interest is that, due to different mechanical behaviours of GFRP, CFRP and stainless steel (STEEL, in the following sections) tendons, the experimental investigation herein summarised allowed to assess the effects of different embedment types on the overall performance of structural LG beam prototypes, including useful considerations on the elastic and post-fracture stages. The presence of relatively short beams (1 m span), in any case, still does not allow to generalise the collected data and observations towards the full development of the design concept, and additional studies are required for large spans, or different geometrical configurations (i.e., number of glass layers, aspect ratio of the LG section, etc.) and mechanical properties (i.e., type of glass and interlayer).

From a qualitative point of view, given the same LG section configuration and dimensions, the introduction of embedded rods with different diameter and material properties first modifies the cross-sectional features of the so-assembled LG-reinforced beams. The R_A ratio of Table 1, in this regard, is used to indicate the resisting cross-sectional area of glass ($A_{glass} = 2 \times 10 \text{ mm} \times 100 \text{ mm}$), compared to the total cross-sectional area of rods (A_{rods}). As far as different materials are accounted for the embedded tendons, moreover, some variations can be expected also in terms of total weight of the beam specimens, as well as total bending stiffness, being emphasised in Table 1 via the R_W and R_{EI} ratios, respectively. Both the R_W and R_{EI} ratios, in particular, are used to denote the increase of weight and expected (elastic) in-plane bending stiffness for the three different series of reinforced beams, compared to the un-reinforced, reference LG specimen.

As shown in Table 1 for the investigated beams, the limited number of embedded rods is not expected to markedly affect their overall weight and stiffness (i.e., with R_{EI} ratios close to the unit). Consequently, mostly identical elastic responses can be reasonably associated to all the beam specimens. Conversely, their post-fracture response is largely dependent on the mechanical features of the rods in use, whose resistance and collapse mechanism directly affect the global bending performance of the tested LG specimens.

3. Simplified analytical modelling

Preliminary analytical calculations, as known, can be useful especially for the design of consolidated structural typologies and can offer reliable estimations, within certain assumptions and limitations.

The simplified calculations reported in this paper are carried out in accordance with the formulations originally presented in [10], where an analytical model was first proposed - in analogy with reinforced concrete theory - to predict the structural performances of LG beams with a stainless steel reinforcement, adhesively bonded at the bottom edge of glass layers. Similar analytical formulations have been presented for glass beams in the literature, focusing on specific structural typologies (see [30–33], etc.).

Based on [10] and adapting the original model to account for multiple embedded rods, in particular, the effective flexural stiffness $EI_{composite}$ of a given LG reinforced glass beam is herein conventionally estimated by considering separately its un-cracked ("A"), cracked ("B") and ultimate ("C") stages (see Fig. 3). In the un-cracked stage, the glass section and the reinforcing rods respond linear-elastically, and the maximum resistance of the full beam is detected as F_1. When the tensile strength of glass is first reached - due to an in-plane bending load according to Fig. 2(c) - the first set of tensile cracks appear in the lower part of glass panels. At this stage ("B" in Fig. 3), the overall load carrying mechanism is basically associated to a compressive force in glass

and a tensile force in the embedded rods, that first manifest their structural contribution for the so assembled LG beam. The reinforced beam is in fact expected to sustain a maximum resistance up to $F_2 > F_1$, depending on the reinforcement mechanical features and capacity. Finally, see stage "C" in Fig. 3, the rods are expected to collapse or start yielding, depending on their intrinsic mechanical features. The ultimate failure of the beam occurs - ideally for a maximum load $F_3 > F_2$ - either when the tensile strength of rods or the compressive strength of glass is reached first.

For the LG specimens herein discussed, a characteristic tensile bending resistance of glass f_t of 45 MPa [23] was taken into account for comparative calculations, with input mechanical features of rods listed in Table 1. In terms of compressive resistance of glass f_c, a conventional value of 450 MPa was taken into account (i.e., that is 10 times the tensile resistance), despite the high variability and uncertainty on such a strength parameter. While design standards for glass suggest a resistance in compression 1000 MPa (see for example [24]), such a nominal value can be affected by several aspects. Experimental studies of literature, in this regard, resulted in average compressive strength values for AN glass in the order of 490 MPa [34]. Such a strength value further decreases in the case of solid glass bricks, i.e. in the order of $\approx 100–120$ MPa (see for example [35,36], etc.).

Actually, the presence of multiple embedded rods was analytically accounted in the form of a single, equivalent tendon (with cross-sectional area given by the sum of three separate rods, see Table 1).

For the modelling approach proposed in [10] and herein adapted to LG-embedded sections, moreover, the structural bending response of the reinforced beams is predicted by assuming that the following hypotheses are valid:

- glass is characterised by a perfectly linear-elastic response
- the reinforcement has a linear-elastic or an ideal elasto-plastic behaviour, in the case of GFRP/CFRP or STEEL specimens, respectively (material properties reported in Table 1);
- the reinforcement is rigidly connected to the glass layers, hence the flexibility of SG foils is fully disregarded and a coupled mechanical interaction is accounted at the glass-to-rods interface;
- plane sections remain plane after bending (Navier-Bernoulli assumptions);
- strains in the glass plates and in the rods are distributed according to the reference analytical model recalled in Fig. 3(b).

Given the geometrical and mechanical features of Fig. 2 and Table 1, the mid-span vertical displacement u of a simply supported reinforced LG beam under four-point bending (i.e., the reference test setup of Fig. 2(c) can be hence expressed as:

$$u = \frac{0.5P \; a_{setup}}{24EI_{composite}}(3L_{setup}^2 - 4a_{setup}^2), \tag{1}$$

where:

a_{setup} represents the distance between the load introduction and the beam end support (see Fig. 2(c),

L_{setup} is the distance between the beam end supports (see Fig. 2(c),

$P = F/2$ is the applied vertical load, and

$EI_{composite}$ is the flexural stiffness of the so assembled, reinforced beam.

Such an $EI_{composite}$ value must be separately calculated for the "A" to "C" stages respectively, so to account for the progressive damage propagation in the given components.

Specifically, in the uncracked stage ("A"), the flexural stiffness of the LG assembly is given by:
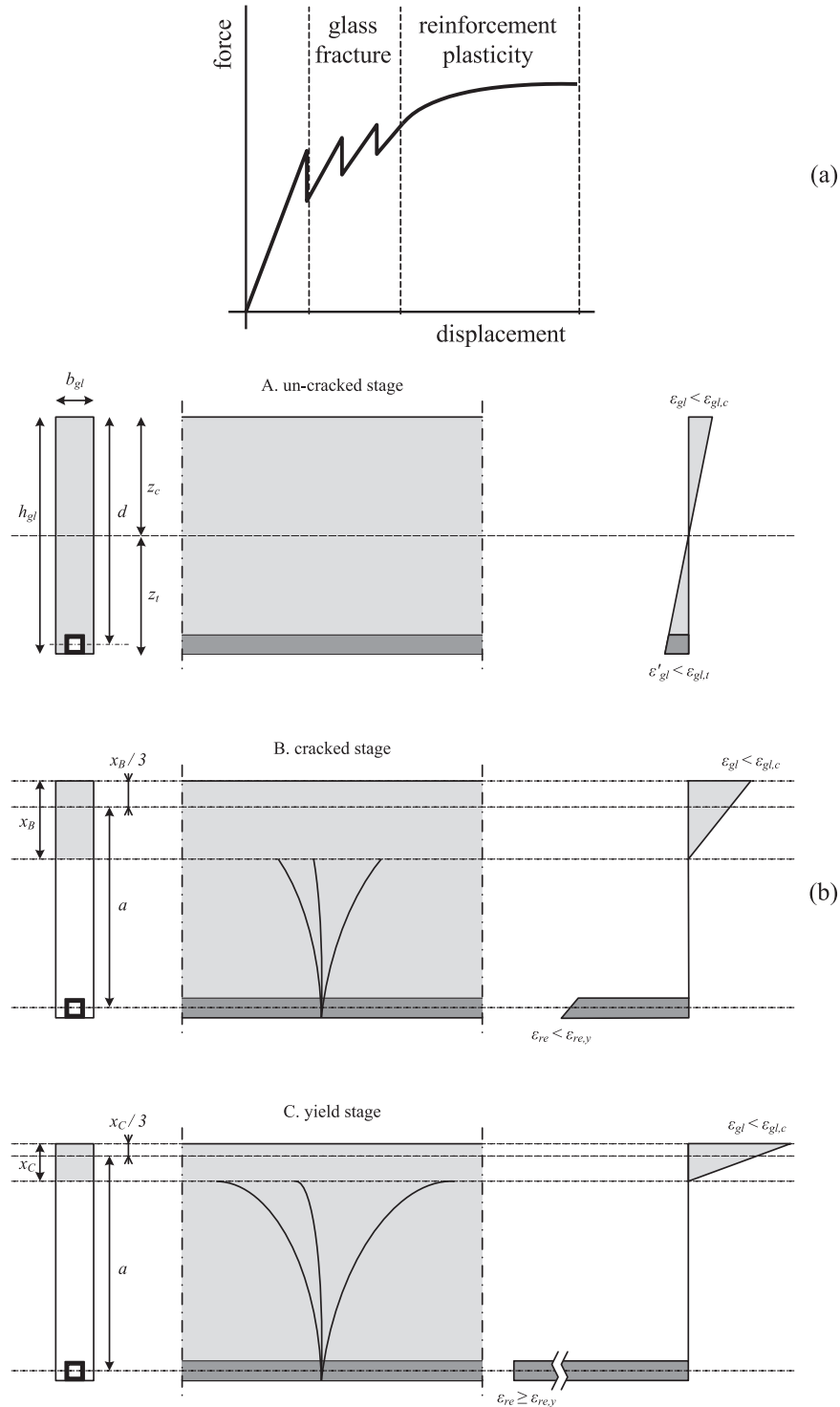
Fig. 3. (a) Typical force-displacement response and (b) stress distribution in the beam components, as discussed in [10] for glass beams with steel hollow re-inforcements. Pictures reproduced from [37], with permission from Elsevier Ltd, Copyright © license n. 4378160384347 (June 2018).

$$(EI_{composite})_A = E_{glass} \sum_{i=1}^{n} \left(I_{y,i} \frac{E_i}{E_{glass}} + z_i^2 A_i \frac{E_i}{E_{glass}} \right)$$

(2)

where:

i represents the considered component (glass or reinforcement) in the cross section

n is the total number of structural components in the cross section ($n = 2$, in this case),

z_i defines the distance between the axis of the i-component and the neutral axis of the

composite beam section,

A_i is the cross-sectional area of the i-component,

E_i the modulus of elasticity of the i-component,
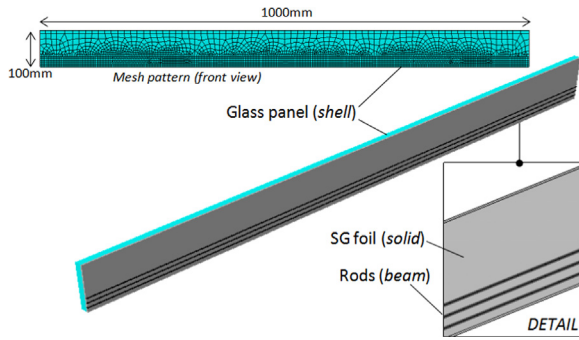
$I_{y,i}$ is the moment of inertia of the i-component.

Fig. 4. Overview of the typical FE model representative of half beam specimen (ABAQUS).

As far as the tensile strength of glass is exceeded ("B"), the stiffness of the beam decreases, since the residual bending capacity of the composite section is provided by a compressive force in glass (i.e. the compressed top edge, for the examined loading condition) and a tensile force in the bottom reinforcement.

In particular:

$$(EI_{\text{composite}})_{\text{B}} = (d - x_{\text{B}})(A_{\text{rod,tot}} E_{\text{rod}})\left(d - \frac{x_{\text{B}}}{3}\right),\qquad(3)$$

with

x_{B} the height of the compressed zone at stage "B", given by:

$$x_{\text{B}} = -\left(\frac{A_{\text{rod,tot}} E_{\text{rod}}}{b_{\text{glass}} E_{\text{glass}}}\right) + \sqrt{2d\left(\frac{A_{\text{rod,tot}} E_{\text{rod}}}{b_{\text{glass}} E_{\text{glass}}}\right) + \left(\frac{A_{\text{rod,tot}} E_{\text{rod}}}{b_{\text{glass}} E_{\text{glass}}}\right)^2},\qquad(4)$$

d the distance between the top of the cross-section and the axis of the (equivalent) reinforcement member,

$A_{\text{rod,tot}}$ the total cross-sectional area of the reinforcement,
b_{glass} the total thickness of glass section,

whereas E_{rod} and E_{glass} are the reinforcement and the glass moduli of elasticity, respectively.

According to Eqs. (3) and (4), it is clear that the analytical estimations are directly related to the input geometrical and mechanical properties of glass and reinforcement components, including the tensile (f_t) and compressive (f_c) resistances of glass.

For the final stage ("C"), the tensile cracks in glass are expected to propagate also in the compressed top edge of the beam. In this latter case, the flexural stiffness of the reinforced cracked section is given by:

$$(EI_{\text{composite}})_{\text{C}} = \frac{9 b_{\text{glass}} E_{\text{glass}} (0.5 P a_{\text{setup}})\left(d - \frac{0.5 P a_{\text{setup}}}{A_{\text{rod,tot}} f_{\text{rod},y}}\right)^2}{2 A_{\text{rod,tot}} f_{\text{rod},y}},\qquad(5)$$

with $f_{\text{rod},y}$ the yielding tensile resistance of the reinforcement.

It is important to notice, at this stage, that since the analytical model accounts for an ideal elasto-plastic response for the reinforcement rods (i.e., as in the case of stainless steel rods), the calculations for GFRP and CFRP specimens were carried out by assuming that the beam collapse is achieved at the end of stage "B", i.e. corresponding with a tensile brittle failure of GFRP and CFRP rods.

4. Finite element numerical modelling

4.1. Modelling approach

The exploratory FE investigation was carried out by taking into account the nominal geometrical and mechanical features of the experimental beam specimens schematised in Fig. 2, including parametric

studies and variations in the configuration of the embedment components, for comparative purposes. In doing so, all the numerical analyses were carried out in ABAQUS, so as to explore the elastic and post-fracture performance of various beam specimens. Major efforts for the parametric FE analyses were derived from earlier research studies, where computationally efficient numerical models have been presented to explore the load bearing capacity of structural glass beams with several reinforcement types.

In this study, the three beam specimens typologies were separately investigated, by means of dedicated FE models. Given the same basic assumptions for the typical model assembly, as well as for the loading protocol and for the material properties, major variations in the set of FE simulations were mostly represented by the features of the rods, according to the geometrical and mechanical data summarised in Table 1. Basically, half specimen was described in each one of these FE models, by taking into account the longitudinal plane of symmetry of the experimental beams (see Fig. 4), with appropriate nodal boundary conditions. The full test setup of Fig. 2(c) was then also reproduced in the form of equivalent nodal restraints for all the FE components.

In accordance with [17], a combination of 3-node and 4-node monolithic shell elements (S3R and S4R type of ABAQUS library) was used for the description of both the 10 mm thick glass panels. Nominal dimensions and thicknesses were accounted for all the FE components. 8-node solid brick elements were indeed used for the description of the SG foils (C3D8R type), so as to physically host the embedded reinforcing tendons. For the rods, finally, beam elements (B31 type) were used, with nominal cross-sectional properties given in Table 1 and Fig. 2(a). Both the mesh pattern and size were properly optimised, based also on past literature efforts, so that reliable predictions on the qualitative crack propagation in glass could be obtained. Given the test setup of Fig. 2, special care was focused on the possible tensile fracture of glass in the bottom region of beams. As such, the edge size of mesh elements, as well as for their aspect ratio, was selected on the base of preliminary sensitivity studies, so that the computational efficiency of the typical FE assembly could be preserved. More in detail, the average mesh size of mesh was refined especially in the beam region subjected to tensile stresses (with 2 mm the average length of shell and solid elements), and increased up to 15 mm for the top/lateral beam regions mainly subjected to compression stresses. The so assembled reference FE model consisted in 6000 elements and 33,000 degrees of freedom.

The numerical description of structural interaction between all the FE model components require then dedicated efforts. Fully rigid, surface distributed "tie" constraints were used at the SG-to-glass interfaces. Such an assumption is in line with most of the FE literature studies on LG glass composites (see [37–43], etc.), and provides reliable predictions as far as severe debonding phenomena are not relevant, as in the case of the experimental investigation herein discussed. Special care for the FE modelling of mechanical interactions, otherwise, should be spent to account for possible local effects, especially in the case of complex glass systems under impact, as well as connections for glass applications (see [44,45], etc.).

Regarding the SG-to-rods mechanical interaction, the "*embedded*" constraint option was used, so that each rod could be physically hosted by the volume of the surrounding SG layers. The "embedded" constraint, conventionally used to model rebar reinforcements within a solid structural component (see [46–48], etc.), assumes that the hosted elements can accommodate the deformations of the hosting region, and no bond-slip phenomena are allowed at their interface. The key assumption of such a FE modelling approach, consequently, is that no relative deformations can occur for the embedded components, with respect to the host element. For the examined set of LG beams, the reliability of the "embedded" constraint was assessed towards past pullout test results of literature, carried out for similar solutions. In [16], more in detail, it was shown that GFRP or CFRP round rods embedded within SG layers can sustain, at room temperature, maximum tensile loads in the order of 3.2 kN, before bond-slip phenomena could

manifest. The post-processing phase of the parametric FE data herein summarised was hence aimed to check also such a limit condition (see Section 5).

A set of displacement-controlled simulations was carried out in ABAQUS/Explicit, in the form of dynamic analyses with quasi-static increase of imposed vertical displacements. Compared to other solving techniques, the Explicit approach is highly time consuming, due to energy balance requirements and mesh size effects (see for example [37,38,41], etc.). In some studies of literature, in this regard, it was shown that a sequence of combined Implicit and Explicit steps can allow to reduce such a typically severe computational cost. This is particularly advantageous when initial predefined conditions (i.e., pre-stress, geometrical imperfections, etc.) are considered within the full loading protocol (see [43], etc.).

The bending test setup of the experiments schematised in Fig. 2, finally, was taken into account via equivalent nodal boundary conditions. The assigned bending deflections, in particular, were linearly increased up to a conventional value of 100 mm (i.e., 1/10 the total span of each sample). This ultimate value was defined – for numerical purposes - as a reference displacement able to ensure the full propagation of damage in all the FE beam components. In doing so, all the simulation were hence processed by monitoring some key aspects of the load bearing performance for the given set of beams, such as:

- the evolution of reaction forces in the region of supports,
- the mid-span deflection increase,
- the stress distribution in each beam components, and
- possible damage initiation/propagation (see Section 4.2 for details on materials).

4.2. Input features

Given the imposed maximum deformation of 100 mm, the full post-fracture performance of the FE models according to Fig. 4 was continuously monitored, starting from their early bending stage. In doing so, the ultimate failure configuration of each beam was numerically detected by accounting for several possible mechanisms that could occur in the structural components, through the in-plane deformation of the beams. Careful consideration was spent especially for a combination of damage effects, namely represented by:

- glass tensile fracture,
- damage in the embedded rods, being associated to a tensile brittle failure (for the GFRP/CFRP tendons) or a progressive yielding and rupture (for the STEEL rods),
- a non-linear response of the SG foils, as obtained on the base of experimental stress-strain input data derived from literature.

Based on the experimental observations briefly discussed in Section 5.1, in addition, possible lateral-torsional buckling phenomena or shear failure mechanisms of the examined beams were considered to have limited influence on the in-plane bending numerical results. Such a conclusion is also supported by the lateral supports schematised in Fig. 2(c), being able to brace the total span of the tested beams and hence to increase up to three times their theoretical lateral-torsional buckling capacity.

In doing so, the possible debonding of the embedded rods from the hosting SG layers was implicitly monitored - through the full FE study - by checking the evolution of tensile forces in each rod. The post-processing analysis of the collected numerical results, in particular, typically emphasised maximum forces in the rods in the order of 3 kN, hence not exceeding the reference pull-out test resistances reported in [16] and allowing to reasonably disregard any kind of bond-slip effects, for the explored beams.

Major advantage in capturing the mentioned damage mechanisms was in fact represented by the implementation of reliable material

mechanical models, for the loading and boundary conditions of interest in this paper. To this aim, past literature efforts related to FE damage modelling in LG assemblies and hybrid systems, as well as experimental performance of small-scale specimens and materials, were taken into account.

In the case of annealed glass, in particular, the *brittle cracking* damage model was used. In accordance with the existing material product standards and past research studies (see for example [37,38], etc.), the nominal mechanical properties were taken into account (f_t = 45 MPa, E_{glass} = 70 GPa, ν_{glass} = 0.23). For FE parametric purposes, such a set of characteristic resistance and elasticity values were uniformly distributed in the thickness of all the glass panels. Further strain-rate effects on the mechanical features of glass were also disregarded, in this research study. In terms of numerical modelling of structural glass systems, past literature investigations showed that a random field distribution of tensile strengths for glass, or the assumption of random critical strain/resistance values in the tensile regions, sometimes can allow for a more realistic simulation of crack initiation (see for example [49–52]). Such a result can be particularly useful when qualitative crack patterns are compared, or for the assessment of glass systems under severe impact, where the opening of first cracks severely affects the overall bending/resistance responses of these systems. Otherwise, it is also known that minimum variations can be typically perceived in terms of post-cracked load-bearing performance of glazing assemblies. In this paper, as the main focus of the investigation was represented by the post-fracture load-bearing response assessment of LG beams (rather than a detailed prediction of their initial fracture patterns), such a random field distribution of material properties was hence reasonably neglected.

Given the above assumptions, in addition, special care was spent on the post-processing phase of the FE predictions, due to the lack - within the used *brittle cracking* option - of compressive resistance limits, compared to the concrete damaged plasticity option [30] or other damage constitutive materials. The potential evolution and propagation of compressive stress peaks in glass was hence continuously monitored, especially close to the end supports and in the central top region of the examined beams, according with the test setup of Fig. 2. The reference damaged configuration in compression was indirectly detected – from FE estimations - by accounting for a compressive strength of glass equal to f_c = 450 MPa. For the post-fracture behaviour in tension, otherwise, major advantage was taken from damage constitutive laws, where the material input calibration - including its *brittle shear* and *brittle failure* sub-options - was derived from earlier research applications to glass beams (with G_f = 3 J/m² the fracture energy and u_{lim} = 1.33 × 10⁻³ mm the failure displacement [37,38], etc.).

For the SentryGlas® adhesive layers, in accordance with [26,45], a non-linear stress-strain constitutive law was considered to account for the average time-loading and temperature conditions of the full-scale experiments (with 20 MPa the corresponding yielding stress), where the equivalent input values of E_{SG} = 120 MPa and ν_{SG} = 0.49 were considered for the MOE and the Poisson' ratio.

Careful consideration was finally spent for the mechanical description of the GFRP, CFRP and stainless steel rods, being expected to represent a key influencing parameter for the comparative FE simulations and the so derived post-fracture observations. In the case of the GFRP and CFRP rods, their typical tensile brittle elastic constitutive behaviour was reproduced by means of an equivalent elasto-plastic stress-strain relationship. In doing so, given the nominal mechanical properties of materials reported in Table 1, a tensile damage criterion was properly calibrated in ABAQUS, via the *ductile damage* material option, so that the single rod in bending could manifest a pure tensile brittle collapse when first achieving its ultimate tensile resistance/strain. Due to the expected tensile brittle performance of the GFRP and CFRP rods in use, in addition, a null plastic capacity was accounted in the so defined constitutive laws, with $f_{rod,y}$ = $f_{rod,u}$ (see Table 1).

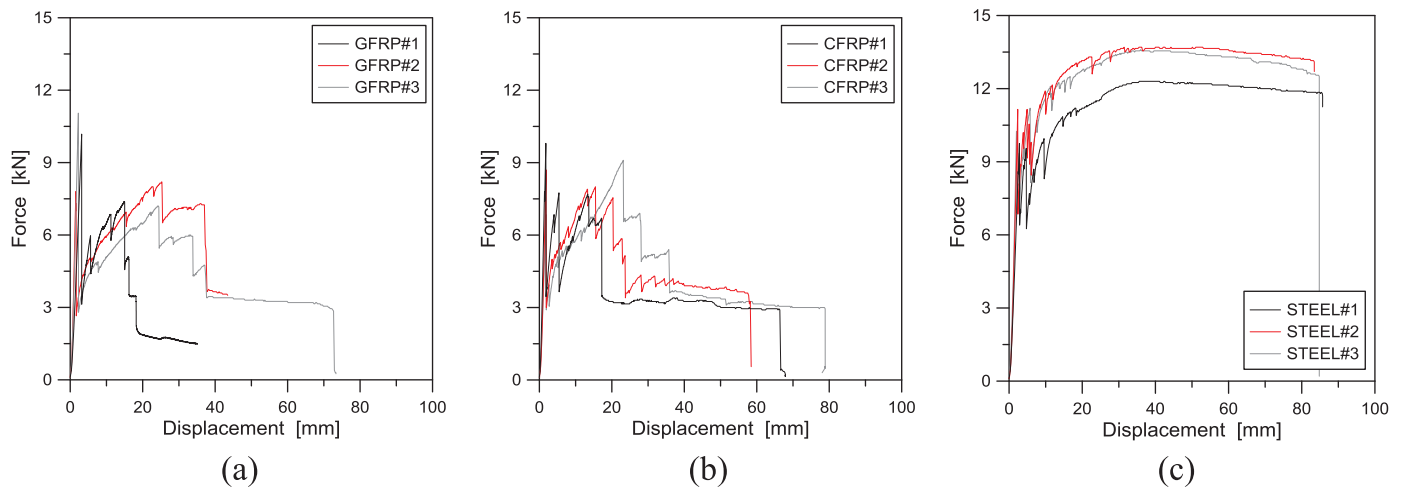This is not the case of the steel rods, where a ductile elasto-plastic

Fig. 5. Experimental force-displacement measurements for LG beams with embedded rods: (a) GFRP, (b) CFRP and (c) STEEL beam specimens.

constitutive law with hardening was implemented, based on the nominal material properties summarised in Table 1.

5. Experimental, analytical and finite element numerical results

5.1. Observations from tests and preliminary analytical calculations

5.1.1. GFRP-reinforced beams

All the tested GFRP-reinforced beams showed a linear-elastic response until the first V-shaped crack, that occurred at an average load of 9.8 kN (± 1.4 kN). A certain dispersion was observed for the GFRP specimens in terms of initial fracture load of glass, namely comprised between 8.0 kN (GFRP#2 specimen) and 11.2 kN (GFRP#3 specimen), corresponding to mid-span beam deflections in the range of 1.5–2 mm (4.30 kN/mm the mean value for the beam elastic stiffness, calculated as the slope of the force-displacement experimental curves).

The predicted range for initial fracture loads recalls the typical variability of glass tensile resistance, and is in line with literature background ([9], etc.).

Worth of interest, see Fig. 5(a), is the post-fracture response of the same beams, where the benefits of the additional embedded rods are exploited, compared to traditional LG sections typically characterised by null plastic capacities (see for example [37,39,43]). According to the analytical models of Section 3, lack of embedded rods would have in fact result in a "phase A" brittle elastic response.

While the post-fracture stiffness of the composite specimens markedly decreases, compared to their elastic stage (≈ 0.19 kN/mm, from the force-displacement curves of Fig. 5(a)), the beams proved to sustain loads up to maximum deflections in the range from 15 to 25 mm, that is 10 times the initial cracking deflection.

Generally speaking, in this regard, the GFRP beam tests highlighted promising benefits, even in presence of reinforcement rods with tensile brittle behaviour. Once the first crack opened in the GFRP specimens, running up to about 93–95% of the beam height, additional load drops and further progressive cracks were experimentally observed for all the specimens, up to collapse. Globally, lack of visible debonding phenomena in the top region of glass in compression proved the efficiency of a certain bridge effect for the residual resistance of specimens, even characterised by marked decrease in the post-fracture resistance and stiffness of the composite specimens. Within the set of GFRP-reinforced beams experiments, additional time was then required for the interpretation of GFRP#1 test results, being characterised by limited post-fracture resistance/deformation capacity, compared to the other specimens (see Fig. 5(a)). Such an experimental outcome - given the observations of qualitative similar damage mechanisms and in-plane bending performances for the three GFRP specimens - was justified in

possible manufacturing issues in the GFRP#1 assembly (i.e., initial imperfections, rod misalignments, lamination, etc.). Despite the limited amplitude of plastic deformations of the GFRP#1 beam, compared to the other specimens, a load-deflection trend and residual stiffness for the cracked section in close correlation with GFRP#2 and GFRP#3 specimens were in fact experimentally estimated. In Fig. 5(a), major loading drops can be easily detected in the post-fracture stage of the GFRP#2 and GFRP#3 beams, for vertical deflections in the order of 40 mm, being representative of the tensile failure of the bottom GFRP rods in bending.

5.1.2. CFRP-reinforced beams

Basically, the CFRP beam specimens offered an in-plane bending performance in close correlation with the GFRP specimens, due to similarity in material properties and nominal size of the embedded rods, see Fig. 5(b). Similar to the GFRP specimens, the initial glass fracture was achieved at a mean deflection of 1.96 mm (1.84 mm and 2.20 mm the limit values), for an average load of 8.6 kN (± 1.2 kN). After the initial linear-elastic response (4.31 kN/mm the experimentally derived elastic stiffness of the specimens), a certain dispersion was again observed in the post-fracture performance of the #1-to-#3 CFRP specimens, in terms of force-displacement comparisons, even in presence of a rather stable post-fracture stiffness for the full set of beams (see Fig. 5(b)).

The maximum ultimate resistance was recorded for the CFRP#3 specimen (9.1 kN at 28 mm of deflection, +5.8% the mean fracture load), while the CFRP#1 and CFRP#2 specimens attained 7.8 kN and 8 kN respectively, at 15 mm and 20 mm of deflection. This means that the CFRP#3 beam sustained the imposed loads up to ≈ 15 times the first cracking deflection, before that the residual capacity could reduce (≈ 8 and ≈ 12 the calculated ductility ratios for the CFRP#1 and #2 specimens). Globally, the cracked stiffness of the CFRP-reinforced beams was calculated in 0.27 kN/mm.

In the specific case of the CFRP#3 beam, however, some possible local effects could have affected such a positive failure prediction. The CFRP#3 specimen, in particular, cracked before the other specimens (7 kN the imposed load at fracture, with 3.8 kN/mm the corresponding beam stiffness). As also perceived from Fig. 5(b), a partial increase of the post-fracture stiffness was then observed for the same specimen, first calculated in 0.15 kN/mm (range of deflections from 5 to 15 mm), and growing up to 0.24 kN/mm (range of deformations from 20 to 28 mm). This effect (+ 60% of stiffness) is counter-intuitive, due to the progressive damage propagation in the beam components, especially the glass panels. Otherwise, it could be justified by possible misalignment of the beam specimen within the test setup, including contact and friction between the glass panels and the steel lateral supports
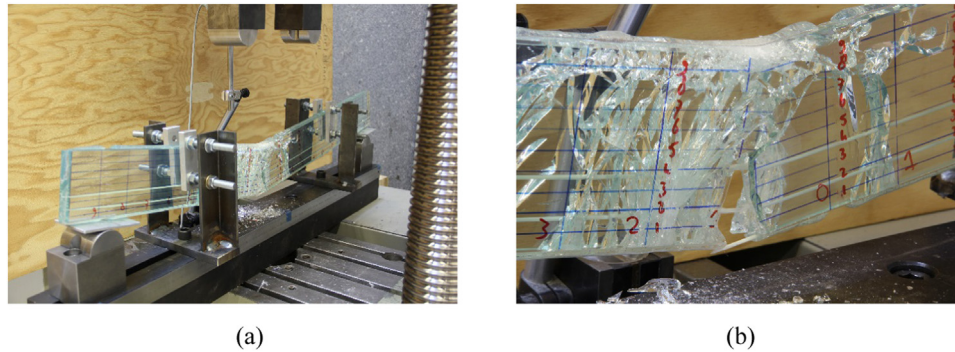
(a)

(b)

Fig. 6. Failure configuration of the GFRP reinforced beams. (a) General view and (b) detail.

specimen. Unfortunately, however, the available experimental measurements do not allow for further confirmation or elaboration of such a kind of explanation.

The tensile failure of CFRP rods governed the collapse mechanism of the beam specimens, even if further major loading drops were also experimentally detected in the force-displacement curved of Fig. 5(b), as a possible result of glass cracks or rods failure.

In any case, the CFRP beam specimens showed some potential for the post-fracture performance enhancement of the traditional LG beams, as it is possible to perceive from Fig. 5(b) after the first cracking peaks. Globally, mostly similar collapse configurations were experimentally observed for GFRP and CFRP beam specimens, see Figs. 6 and 7.

5.1.3. STEEL-reinforced beams

Finally, as expected, major benefits due to embedded rods for the post-fracture beam performance were experimentally observed for the STEEL series, see Fig. 5(c). For the steel reinforced beams, the initial glass failure occurred at an average value of 10.4 kN (± 0.5 kN), at a mean deflection of 2.3 mm, followed by a markedly stable post-fracture bending behaviour, especially with respect to the GFRP and CFRP specimens.

The elastic stiffness of the STEEL beams (mean value) was experimentally calculated in 4.36 kN/mm, which is in line with the GFRP and CFRP set of beams and with the design expectations, due to the limited amount of embedded rods (see also Table 1).

In terms of post-fracture observations, minor loading drops associated to the progressive opening of additional cracks in glass proved to have limited effects on the overall stability of the STEEL specimens, taking advantage of steel rods. The beam stiffness derived from the force-displacement experimental measurements resulted in a mean value of 0.15 kN/mm, in the cracked range comprised between 15 and 25 mm, hence still in line with the GFRP and CFRP specimens. Major effects of STEEL rods were manifested after yielding of reinforcements, leading to a progressive increase of the sustained load and to large

deformations. All the STEEL specimens reached in fact the maximum displacement allowed by the test setup (i.e., 100 mm, that is ≈ 45 times the deflection at first cracking), still carrying on a total load of about 13.0 kN (+ 25% the initial fracture load). When the tests were stopped, the compression zone of the glass was damaged but still in place. However, when the beams were unloaded, local explosive failure of the glass occurred in their mid-span compressed region, and only the SG interlayer foils remained in place (see Fig. 8). Such a kind of phenomenon, given a mostly gradual unloading phase for all the experiments, can be reasonably explained in the form of a local instability of glass fragments, as an effect of a loading magnitude variation for the cracked beams.

5.1.4. Analytical assessment of test results

A further comparison between the structural response of the three beam types is collected in Fig. 9 and Table 2, where the load-displacement curves and some major key parameters for their bending performance (F_1, F_2 and F_3 loading values according to Section 3) are reported, with the corresponding analytical estimations.

Given the F_i values in Table 2, in particular, from the test data it is possible to notice that the GFRP, CFRP and STEEL beams can apparently offer a similar maximum resistance at the first glass cracking (avg (F_1)), for all the set of beam specimens. This is also in line with the elastic stiffness calculations previously derived from Fig. 5, and is strictly related - even in presence of an intrinsic variability in the actual tensile resistance of glass [9] - to the limited number of rods, with respect to the LG un-reinforced section (i.e. Table 1).

However, a totally different post-fracture resistance and ductility is associated to the overall bending performance of the same beams. Such an effect mostly results from yielding and plastic deformations of the STEEL reinforcements, which are absent for the CFRP and GFRP beam specimens, see Fig. 9.

In terms of analytical modelling, it can be noticed that the simplified calculations according to Section 3 can roughly capture the first cracking condition for the examined specimens. In addition, the same
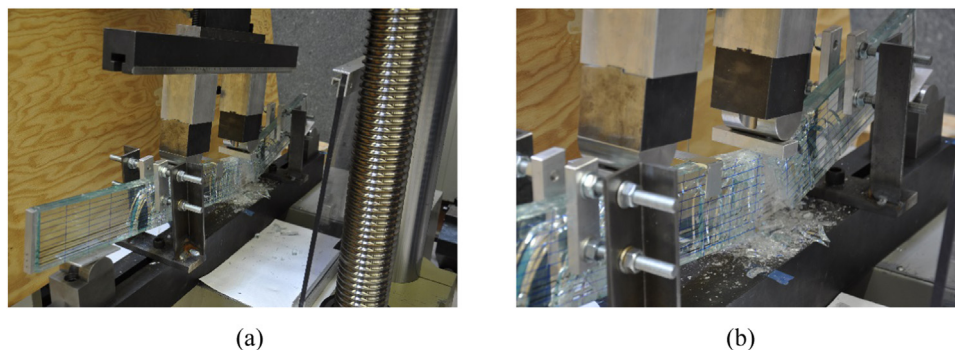

(a)

(b)

Fig. 7. Failure configuration of the CFRP reinforced beams. (a) General view and (b) detail.
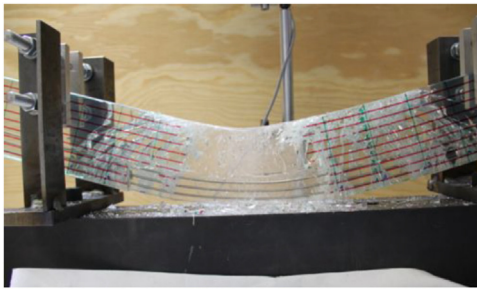
Fig. 8. Failure configuration of the STEEL reinforced beams (front view).

formulation is not able to predict the overall bending performance of the examined specimens, as a direct effect of its simplified assumptions, as well as of possible variations in the mechanical properties of the involved materials, herein assumed in their nominal values according to Table 1. The major limit of the analytical estimations is given by the rough description - within the simplified model - of post-cracked contributions that can be typically observed from the corresponding full-scale experiments, as far as damage in glass progressively occurs in the form of distributed and/or major cracks. The actual effect is a severe (even conservative) underestimation of the post-fracture residual resistance and stiffness for the examined assemblies. According to Table 2, in particular, such an assumption resulted in cracked resistance scatters in the order of −80% the corresponding F_2 test results.

More in detail, the structural response of the GFRP and CFRP series reported in Fig. 9 and Table 1 are very similar. Minor variations in their overall response were justified by intrinsic features of embedded rods, as well as possible scatter in nominal mechanical properties of glass. After the initial fracture of glass, they both showed residual bending stiffness and they were able to carry an increasing load which reached values close to the initial failure one. Due to the higher modulus of elasticity, the CFRP beams showed a slightly higher stiffness at the fractured stage. Despite that, these beams also showed more irregular load - displacement curves, probably due to the smaller bonding area which seems to have led to a slightly reduced adherence with the SG interlayer. Although both the glass beam itself and the reinforcement rods are made of brittle materials, all specimens showed significant post-fracture redundancy and reached the maximum allowed displacement before complete failure. Nevertheless, the initial failure load was not exceeded by the cracked beams, which would need higher reinforcement rates.

The STEEL beam series showed the best structural response, with a residual strength that reached up to 132% of the initial failure load. The

post-fracture response of the steel reinforced beams was much stiffer than the other beam series. This higher stiffness avoided the localised glass failure experienced by the other specimens. The cracks were in fact evenly distributed along the length of the beam. This led to smooth load - displacement curves and, at the yielding stage, the bending stiffness of the beam gradually decreased without any abrupt drop of the load. When the maximum vertical displacement at mid-span (about 70 mm) was reached, the beams were still carrying a nearly constant load, close to the maximum value. The overall response of the steel reinforced beams can thus be regarded as highly redundant and ductile. This profitable failure behaviour is due to a gradual and evenly distributed cracking of the glass, which gradually weakens the beam thus decreasing its bending stiffness.

The initial failure load proved to be always overestimated by the analytical model. A marked load drop, in particular, follows the initial glass fracture, due to the rather coarse reduction in the post-fracture bending stiffness that is assumed by the adopted analytical model, for the examined composite sections. Such a reduction appeared to be actually slightly more gradual, probably due to a small contribution of the SG interlayer. Worth of interest is the stiffness of the fractured beams, giving evidence of rather close correlation with the analytical predictions, for all the specimens.

For the GFRP and CFRP beam series, the load at which the first reinforcement failure occurred, was precisely predicted too. After that, however, the experiments showed significant plastic deformations, probably due to the bond-slip contribution of the SG foils, which is not taken into account by the analytical calculations. The maximum post-fracture load, in addition, was very precisely predicted for the two first beam series, but at the same time it was significantly underestimated for the STEEL specimens. Such a result could derive from hardening effects of steel rods after yielding, which are not taken into account by the analytical model, where an elastic-perfectly-plastic behaviour was assumed for them. It is however difficult to say if this is also caused by inaccurate material parameters, since it was not possible to actually test the reinforcement rods.

Despite such a series of observations and comparisons, the analytical results can offer some useful outcomes, at least for preliminary design considerations. It is worth mentioning that the current study explored the effect of embedded rods on the bending performance of double LG section prototypes. In this regard, similar benefits are expected to be achieved for LG beam sections resulting from real design processes, where – according to design standards and guideline documents (see for example [9]) – at least three glass layers (and hence two foils for embedding the reinforcing rods) are used. In all these cases, the capacity of carrying higher loads than the initial failure load would
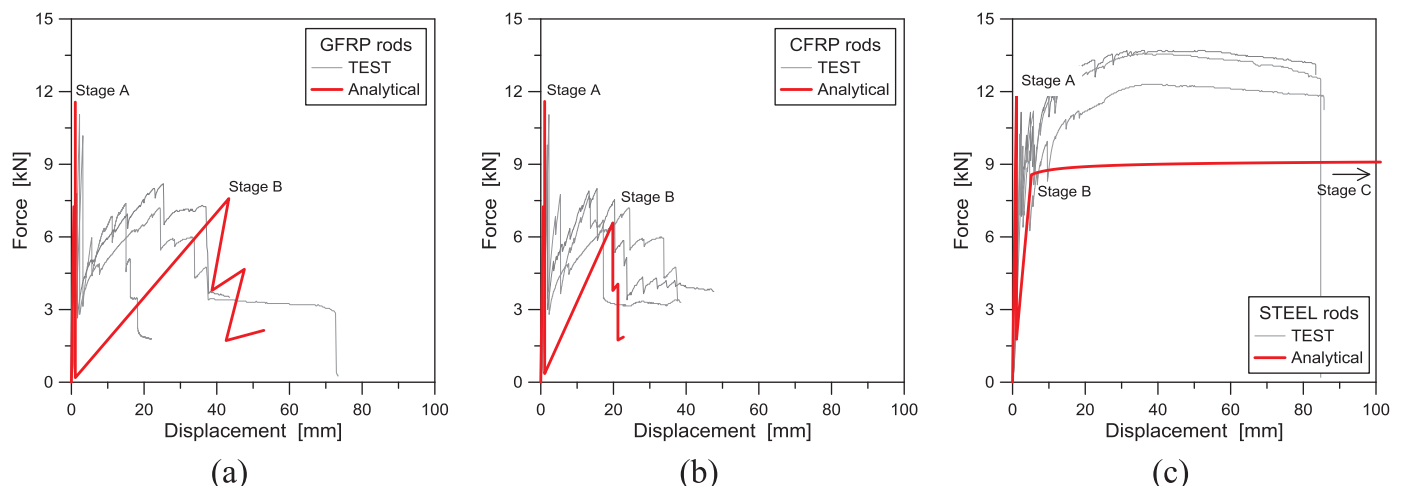

Fig. 9. Experimental and analytical results for LG beams with embedded rods. Force-displacement comparisons for (a) GFRP, (b) CFRP and (c) STEEL beam specimens. Analytical calculations derived from Eq. (1), in accordance with [10].

Table 2
Key performance parameters for LG beams with GFRP, CFRP or STEEL rods, as experimentally and analytically calculated, with evidence of average ('Avg') and standard deviation ('StD') values.

		GFRP				CFRP				STEEL			
		F_1 [kN]	F_2 [kN]	F_3 [kN]	F_3/F_1 –	F_1 [kN]	F_2 [kN]	F_3 [kN]	F_3/F_1 –	F_1 [kN]	F_2 [kN]	F_3 [kN]	F_3/F_1 –
Test	#1	10.2	3.1	7.4	0.7	10.0	3.5	7.8	0.8	10.3	6.9	13.6	1.3
	#2	8.0	2.6	8.2	1.0	8.9	3.0	8.0	0.9	11.2	6.8	13.7	1.2
	#3	11.2	2.8	7.2	0.6	7.0	2.9	9.1	1.3	9.9	6.4	12.3	1.3
	Avg	9.8	2.8	7.6	0.8	8.6	3.1	8.3	1.0	10.4	6.7	13.2	1.3
	StD	1.4	0.2	0.4	0.2	1.2	0.2	0.6	0.2	0.5	0.2	0.6	0
	Analytical	11.6	0.2	7.6	0.7	11.6	0.4	6.6	0.6	11.9	1.8	9.1	0.8
	Δ	18.4	− 92.8	0	− 12.5	34.9	− 87.1	− 20.5	− 40.0	14.4	− 73.1	− 21.1	− 38.5

$\Delta = 100 \times (y_{Analytical} - y_{Test})/y_{Test}$, with F_1, F_2, F_3 corresponding to stages "A", "B", "C" of Fig. 3.

allow the safe use of glass beams as structural elements. Thus, the most important parameter to predict for the design reinforced glass beams - with safe post-fracture behaviour - is the maximum residual strength. This parameter was very accurately predicted for the first two beam series, while it was significantly underestimated for the last (STEEL) one. This is probably due both to the material parameters that were chosen and to the assumption of elastic-perfectly-plastic behaviour for stainless steel, which is not fully reliable for the high strength, AISI type steel that was adopted at the time of the experiments.

As far as the analytical curves in Fig. 9 are taken into account for preliminary comparative purposes with test results and initial calculations only, a rather good agreement can be in any case noticed, given the simplified assumptions of the analytical model as well as the use of nominal material properties for glass and rods. More accurate estimations and local investigations require indeed FE numerical modelling and appropriate material damage assumptions.

5.2. Discussion of finite element numerical results

A further attempt to analyse the bending performance of GFRP, CFRP or STEEL beams was carried out via more detailed FE simulations.

In doing so, the reliability of FE input features and assumptions was preliminary assessed, to ensure their correctness. In Fig. 10, for example, the effects of end supports are emphasised, in terms of deformations (Fig. 10(a)) and distribution of local stresses in glass

(Fig. 10(b)). The FE model agrees with Fig. 4 and includes - additionally - the small aluminium plates, that at the time of the experiments were interposed between the LG specimens and the test setup (see Figs. 6–8). There, a view cut (300 mm from the beam lateral edge) is proposed. The aluminium plate is accounted in the form 3D brick elements (70 GPa and 0.23 the MOE and Poisson' ratio respectively), while a *surface-to-surface* contact interaction is used at the LG beam-to-plate interface. In this manner, possible sliding (μ = 0.3 the friction coefficient) and separation of the LG beam, with respect to the aluminium plates, can be taken into account during the bending deformation. Compared to Fig. 10 (where the contour plots are selected at an imposed vertical displacement of 1.5 mm), the use of ideal nodal restraints proved to have minor effects (0.38% the calculated scatter).

As far as the full force-displacement response of the beams is considered, see Fig. 11, a rather close correlation between the proposed FE models and the corresponding test measurements was generally observed.

For the three beam types, in particular, the FE modelling further emphasised that the actual bending response is characterised by the key phases summarised in Fig. 3(a), namely including (i) the elastic stage, (ii) the first cracking phase and (iii) the final collapse.

At the same time, a clear distinction between the post-fracture performance of the same beams was highlighted. Worth of interest, compared to traditional, un-reinforced LG beams (where null ductility can be offered by cracked glass, see for example [10,37,39,43]), is that

(a)

(b)
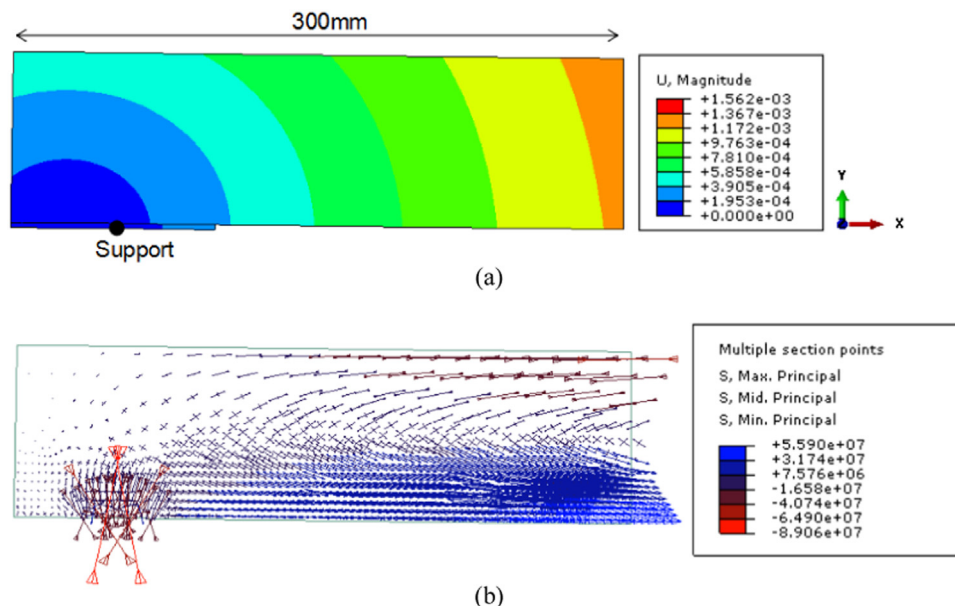
Fig. 10. FE assessment of model restraints on the predicted (a) displacements (values in m) and stresses (values in Pa) in glass (ABAQUS, scale factor = 3).
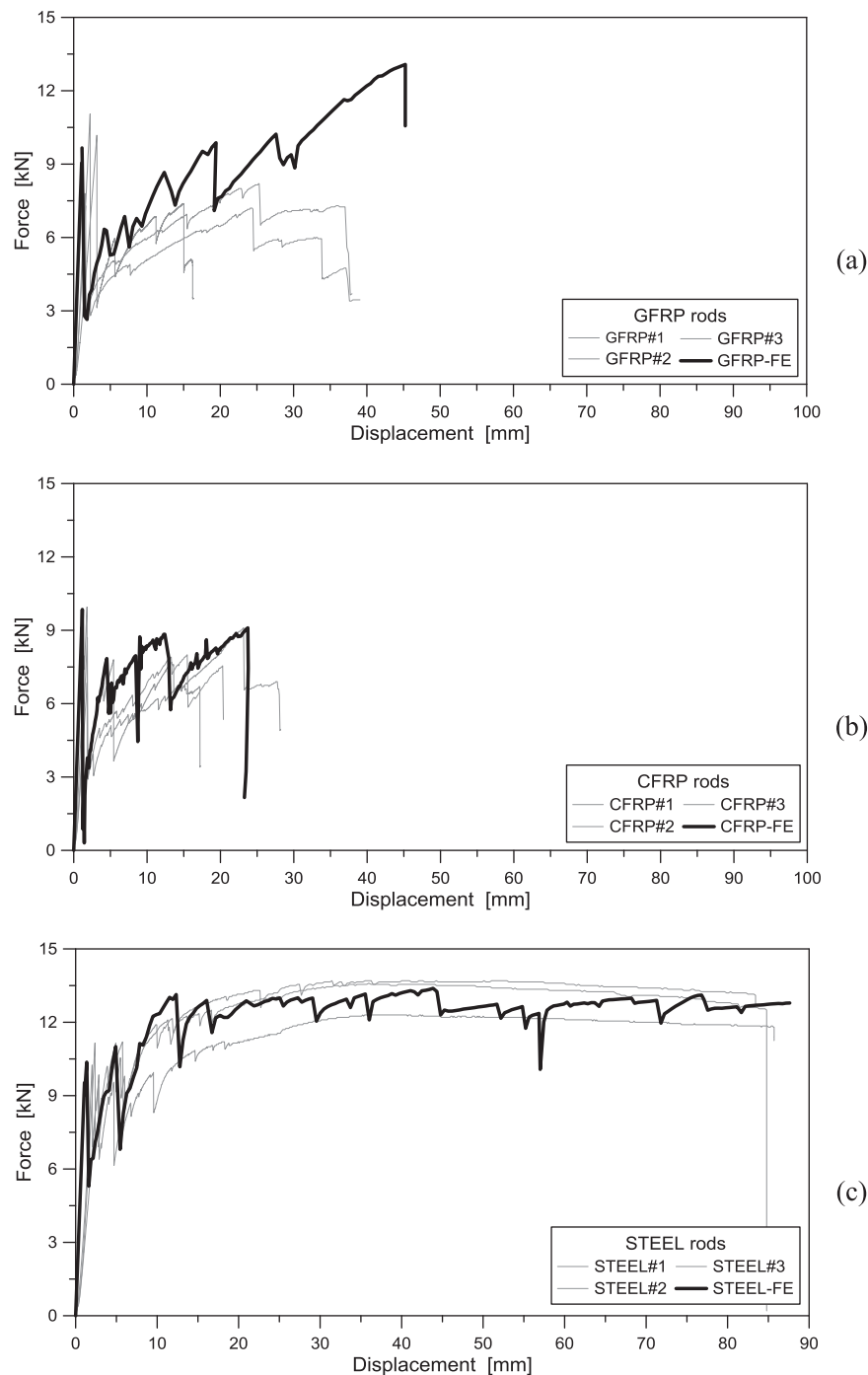
Fig. 11. Numerical (ABAQUS) and experimental results for LG beams with embedded rods. Force-displacement comparisons for (a) GFRP, (b) CFRP and (c) STEEL-reinforced beam specimens.

in any case the embedded rods can offer marked benefits, in terms of residual resistance and maximum deformations in the post-fracture stage, hence resulting in a marked improvement of redundancy and ductility.

Actually, from the numerical and experimental data collected in Fig. 11, it is possible to notice that FE models tend to partly overestimate the elastic stiffness of specimens (up to +10% the scatter with the corresponding experimental values), for all the beam typologies. This scatter, as also in accordance with earlier comparative applications of the FE method to structural glass beams, can be explained by possible local deformations of the experimental setup, being the latter values actually included in the measured vertical deflection of the specimens

control point but not accounted by the corresponding FE models. An additional reason for such a kind of scatter can be represented by possible production tolerances, especially in terms of glass thickness, that could result in $\pm$ 2% variations from the nominal value (and hence in $\pm$ 2% scatter for the predicted FE responses).

In terms of initial fracture load F_1, in addition, it can be seen that the assumption of a nominal value for the tensile resistance of glass generally provides close correlation with experimental average values for F_1, for all the beam types.

Rather interesting correlation was then generally noticed between FE simulations and reference test results, in terms of global bending performance up to collapse of the specimens. Loading drops reported in
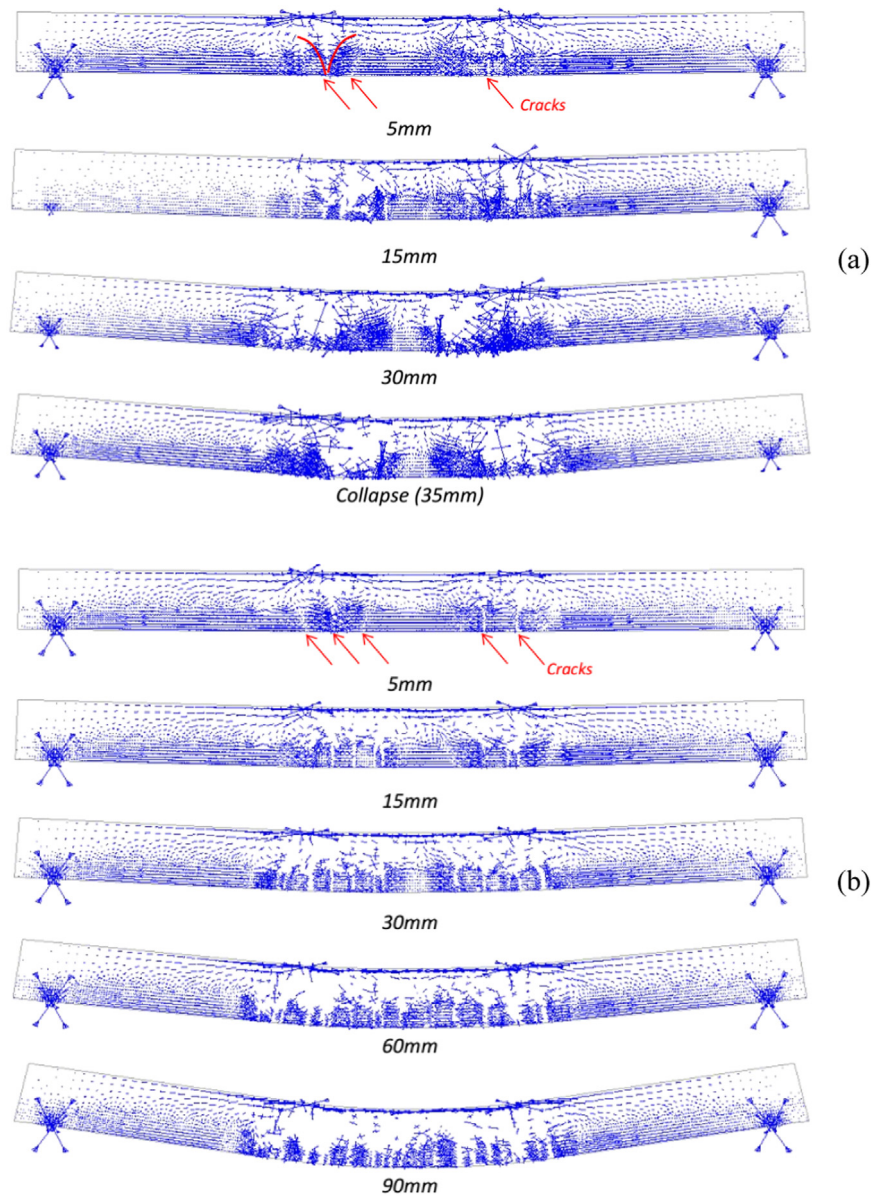
Fig. 12. Numerical results for LG beams with embedded rods. Cracks in glass, as a function of the vertical deflection. (a) CFRP and (b) STEEL beam specimens (ABAQUS).

Fig. 11, in particular, were found to derive from progressive glass cracking, as in the case of the experiments.

Through the post-fracture stage of the simulation process, the actual resistance depends on the limited residual glass section, but takes major advantage from the embedded rods acting as tensile tendons for the fractured beams. As a consequence, the FE specimens of Fig. 11 are able to sustain additional loads as far as the rods themselves do not collapse due to tensile loads. Beside the lack of additional small scale tests on single components, to further calibrate the input material properties for GFRP, CFRP and STEEL rods, it can be noticed in Fig. 11 that the use of nominal material properties for the rods generally proved to estimate with rather interesting accuracy the ultimate configuration of the corresponding experimental specimens, hence suggesting a further extension of the same FE numerical study, aiming to investigate more in detail the potential and actual performance of the examined structural typology. Major scatter was observed especially for the GFRP beams, where the FE models underestimated the ultimate configuration for the experimental specimens.

Besides the mostly different overall bending performance of the

examined beam types, the FE simulations also emphasised a specific (even qualitative) crack scenario for the same specimens, as a function of the mechanical features of the embedded rods. In Fig. 12, selected vectorial patterns of principal stresses in glass are proposed for the CFRP and STEEL beams, as a function of the mid-span vertical deflection. As shown, the stress distribution in glass gives a clear evidence of the propagation of cracks in the glass panels, having a typical V-shape with close correlation with the experimental observations. By comparing the CFRP and STEEL damaged configurations, in addition, a totally different evolution of cracks can be perceived, with the CFRP beam being affected by a limited number of major fractures, while a large number of minor cracks can be noticed for the STEEL beam.

The opening and propagation of cracks also reflects on the evolution of maximum stresses in the other beam components. In Fig. 13, a comparative example is proposed in terms of (a) compressive stresses at the top edge of glass and (b) tensile stresses in the lower tendon (mid-span section), as a function of the beam deflection. The attention is focused on the first 15 mm of deflection, where the transition from the elastic to the cracked stage can be observed. Stress drops are measured
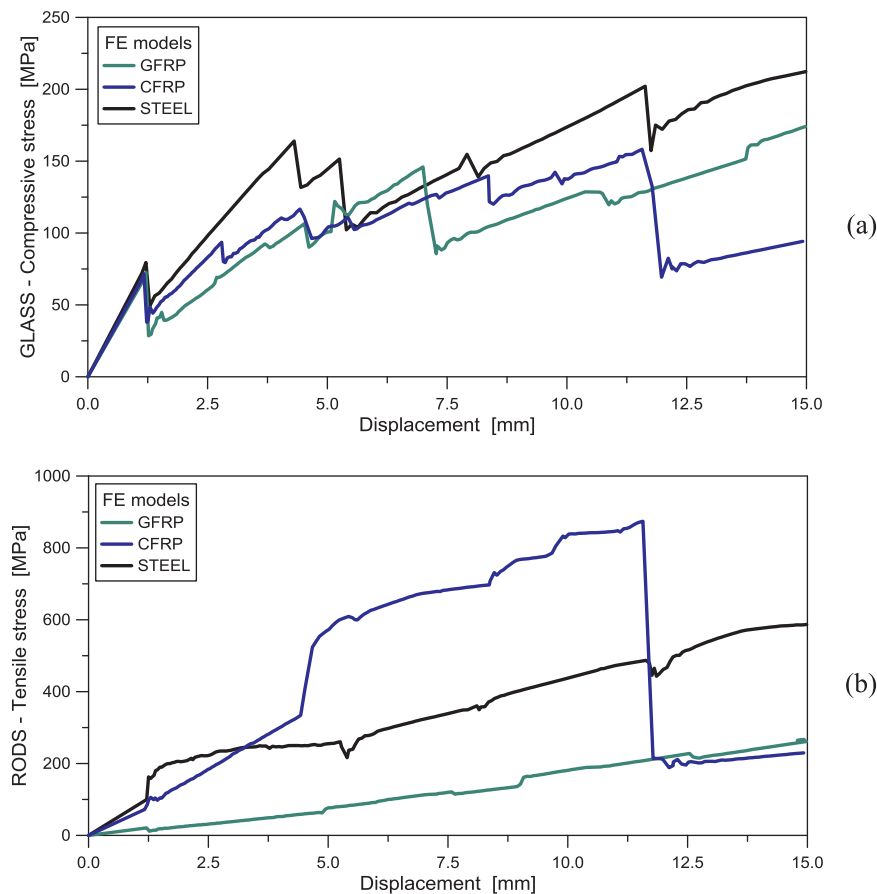
Fig. 13. Numerical comparisons for GFRP, CFRP and STEEL beam specimens: (a) compressive stress at the top edge of glass and (b) tensile stress in the lower rod (mid-span section), as a function of the vertical deflection (ABAQUS).

in the glass plates (see Fig. 13(a)), and are mostly associated to the opening of cracks at their bottom edge. Maximum values up to 250–300 MPa were globally measured, even for large beam deformations. More pronounced effects of progressive cracks can be noticed also in terms of stress evolution in rods, see Fig. 3(b), in the form of non-linear trend for the collected plots. Worth of interest is the qualitative observation that higher stresses are first achieved in the CFRP tendon, i.e. for the beam type offering the minimum post-cracked ductility, compared to GFRP and STEEL samples. Additional research, however, is still required for the design concept herein presented.

6. Conclusions

In this paper, the structural performance of composite laminated glass (LG) beams with embedded reinforcement rods was investigated. Compared to traditional, un-reinforced LG beams, careful consideration was spent on different solutions for the embedded rods in use, being laminated within the typical resisting LG section, and namely consisting of GFRP, CFRP or stainless steel (STEEL) tendons. The attention was focused especially on the post-fracture performance of the so assembled beams, including original laboratory experiments, preliminary analytical calculations and refined finite element (FE) numerical simulations.

Compared to un-reinforced LG beams, typically associated to tensile brittle performances and null plastic capacities (i.e., as a direct effect of glass intrinsic features), the examined embedded solutions proved to offer positive effects in terms of post-fracture residual stiffness, resistance and redundancy.

In particular, from the selected outcomes of discussed experiments, it was shown that the concept of embedded reinforcement is feasible, and should be further investigated for design purposes. Even in

presence of limited sections for the rods ($\approx$ 100–400 the explored range of glass-to-rod cross-sectional ratios), the beam specimens proved to offer significant residual load-bearing capacity. In addition, post-fracture deflections at least equal to 10 times the first cracking deformation of the same beams were experimentally predicted, for beam specimens with typically brittle GFRP and CFRP rods. Such a ductility increase was maximised (with experimental post-fracture deformations up to 45 times the first cracking deformation) for the STEEL specimens. The analysis of relatively short beams (1 m their span), however, actually suggests the need of additional studies on different geometrical configurations, so as to allow generalising the collected data and the well promising observations.

In terms of analytical calculations, the collected predictions for the post-fracture performance of the examined reinforced LG beams gave evidence of certain limits, being strictly related to the basic assumptions of the formulation, hence requiring further modelling efforts and enhancements (i.e., at the material constitutive law side), so as to account for even complex and more realistic damage phenomena in the cracked stage.

The FE numerical investigation, finally, generally resulted in rather accurate predictions for all the examined beam typologies, highlighting a rather good correlation with the test results and further enforcing the presence of a mostly different bending performance for the examined LG beams, as far as even minor modifications are implemented in terms of embedded rods (i.e., mechanical features and geometry). Such a close correlation with the experiments was found to result from the reliable numerical modelling of the beam components, as well as their reciprocal mechanical interaction, as a part of composite assemblies. In this regard, given the well promising in-plane bending performance of the selected beam configurations, further studies will be carried out on

the same design concept, including variations in geometrical and mechanical features, as well as in the reference loading and boundary conditions.

References

[1] S. Moghtadernajad, L.E. Chouinard, M. Saeed Mirza, Multi-criteria decision-making methods for preliminary design of sustainable facades, J. Build. Eng. 19 (2018) 181–190.

[2] A. Piccolo, F. Simone, Performance requirements for electrochromic smart window, J. Build. Eng. 3 (2015) 94–103.

[3] S. Barbosa, K. Ip, Predicted thermal acceptance in naturally ventilated office buildings with double skin facades under Brazilian climates, J. Build. Eng. 8 (2016) 92–102.

[4] I. Pérez-Grance, J. Meseguer, G. Alonso, Influence of glass properties on the performance of double-glazed facades, Appl. Therm. Eng. 25 (17–18) (2005) 3163–3175.

[5] V. Huckemann, E. Borges Leao, M. Leao, Acoustic comfort in office buildings with double skin glass facades, Bauphysik 31 (5) (2009) 305–312.

[6] Z. Huang, M. Xie, J. Zhao, Y. Du, H.-K. Song, Rapid evaluation of safety-state in hidden-frame supported glass curtain walls using remote vibration measurement, J. Build. Eng. 19 (2018) 91–97.

[7] C. Bedon, X. Zhang, F. Santos, D. Honfi, M. Kozłowski, M. Arrigoni, L. Figuli, D. Lange, Performance of structural glass facades under extreme loads - design methods, existing research, current issues and trends, Constr. Build. Mater. 163 (2018) 921–937.

[8] M. Haldimann, A. Luible, M. Overend, Structural Use of Glass. IABSE, ISBN 978-3-85748-119-2, 2008.

[9] M. Feldmann, R. Kasper, B. Abeln, P. Cruz, P., et al. Guidance for European Structural design of glass components – support to the implementation, harmonization and further development of the Eurocodes. Pinto Dimova, Denton Feldmann (Eds.), Report EUR 26439, Joint Research Centre – Institute for the Protection and Security of the Citizen, ⟨http://dx.doi.org/10.2788/5523⟩, 2014.

[10] C. Louter, Fragile yet Ductile: Structural Aspects of Reinforced Glass Beams (Ph.D. Thesis), Delft University oaf Technology, 2011 (ISBN: 9789085707431. Available online (accessed June 2018): uuid: 15375137-d9f6-456d-a4de-df14d167a2d2).

[11] K. Martens, R. Caspeele, J. Belis, Development of reinforced and post-tensioned glass beams: review of experimental research, J. Struct. Eng. 142 (5) (2015) 04015173.

[12] J. Cupac, Post-tensioned Glass Beams (Ph.D. Dissertation), EPFL Lausanne, Switzerland, 2017 10.5075/epfl-thesis-7895.

[13] K. Martens, R. Caspeele, J. Belis, Experimental investigation into the effects of membrane action for continuous reinforced glass beam systems, Glass Struct. Eng. 3 (2018) 389–402.

[14] M. Engelmann, B. Weller, Residual load-bearing capacity of spannglass-beams: effect of post-tensioned reinforcement, Glass Struct. Eng. (2018) https://doi.org/10.1007/s40940-018-0079-4.

[15] C. Louter, High-strength fibre rods as embedded reinforcement in SentryGlas-laminated glass beams, in: Proceedings of Glass Performance Days 2009, Tampere, Finland, ⟨www.glassfiles.com⟩.

[16] C. Louter, C. Leung, H. Kolstein, J. Vamberský, Structural glass beams with embedded glass fibre reinforcement, in: Proceedings of Challenging Glass 2 – Conference on Architectural and Structural Applications of Glass, TU Delft, May 2010, ⟨https://doi.org/10.7480/cgc.2.2341⟩, 2010.

[17] C. Bedon, C. Louter, Numerical investigation on structural glass beams with GFRP-embedded rods, including effects of pre-stress, Compos. Struct. 184 (2018) 650–661.

[18] Simulia, ABAQUS v.6.14 computer software and online documentation, Dassault Systems, Providence, RI, US, 2016.

[19] P.-.Y. Adant, E. Mazzocchi, C. Louter, J.-.P. Lebet, Structural glass beams with embedded reinforcements - analysis on different reinforcement concepts applied to laminated glass beams. Internal Laboratory Report, EPFL/ICOM, Lausanne, Switzerland, 2013.

[20] C. Bedon, J. Belis, C. Amadio, Structural assessment and lateral-torsional buckling design of glass beams restrained by continuous sealant joints, Eng. Struct. 102 (2015) 214–229.

[21] D. Sonck, J. Belis, Elastic lateral-torsional buckling of glass beams with continuous lateral restraints, Glass Struct. Eng. 1 (1) (2016) 173–194.

[22] A. Luible, D. Scharer, Lateral torsional buckling of glass beams with continuous lateral support, Glass Struct. Eng. 1 (1) (2016) 153–171.

[23] EN 572–EN 572, Glass in buildings-Basic Soda Lime Silicate Glass Products, CEN, Brussels, Belgium, 2004.

[24] CNR-DT 210/2013, Istruzioni per la progettazione, l'esecuzione ed il controllo di costruzioni con elementi strutturali in vetro (Technical Document, in Italian), National Research Council, Rome, Italy, 2013.

[25] D. Callewaert, Stiffness of Glass/Ionomer Laminates in Structural Applications (Ph.D. Dissertation), Ghent University, 2011.

[26] M. Santarsiero, C. Louter, A. Nussbaumer, The mechanical behaviour of SentryGlas® ionomer and TSSA silicon bulk materials at different temperatures and strain rates under uniaxial tensile stress state, Glass Struct. Eng. (2016), https://doi.org/10.1007/s40940-016-0018-1.

[27] R&G GmbH®, Chapter 08. Glass, aramid and carbon fibre, R&G composite handbook edition 8, ⟨www.r-g.de⟩. (last: Accessed September 2018).

[28] TOHO TENAX EUROPE GmbH, Datasheet Tenax HT5131, ⟨www.tohotenax-eu.com⟩. (last: Accessed September 2018).

[29] EN 10088-1, Stainless Steels - Part 1: List of Stainless Steels, European Committee for Standardization (CEN), Brussels, Belgium, 2014.

[30] A.B. Ølgaard, J.H. Nielsen, Design of mechanically reinforced glass beams: modelling and experiments, Struct. Eng. Int. 2 (2009) (2009) 130–136.

[31] E. Speranzini, S. Agnetti, Flexural performance of hybrid beams made of glass and pultruded GFRP, Constr. Build. Mater. 94 (2015) 249–262.

[32] B. Abeln, E. Preckwinkel, E. Yandzio, M. Heywood, M. Eliasova, M. Netusil, C. Grenier, Development of Innovative Steel-glass Structures in Respect to Structural and Architectural Design (Innoglast), Report EUR 25316 EN, (2013), https://doi.org/10.2777/91697.

[33] G. Campione, Flexural behavior of glass beams with T and I shape cross-sections, J. Struct. Eng. 143 (9) (2017), https://doi.org/10.1061/(ASCE)ST.1943-541X.0001836.

[34] A. Fink, Ein Beitrag zum Einsatz von Floatglas als Dauerhaft Tragender Konstruktionswerkstoff im Bauwesen (Dissertation), Technische Universitat Darmstadt, Institut fur Statik, 2000 (ISSN 1433-7789).

[35] G. Royer-Carfagni, M. Silvestri, A proposal for an arch footbridge in Venice made of structural glass masonry, Eng. Struct. 29 (11) (2007) 3015–3025.

[36] F. Oikonomopoulou, F. Veer, R. Nijsse, K. Baardolf, A completely transparent, adhesively bonded soda-lime glass block masonry system, J. Facade Des. Eng. 2 (2014) (2014) 201–221.

[37] C. Bedon, C. Louter, Exploratory numerical analysis of SG-laminated reinforced glass beam experiments, Eng. Struct. 75 (2014) 457–468.

[38] K. Martens, R. Caspeele, J. Belis, Numerical investigation of two-sided reinforced laminated glass beams in statically indeterminate systems, Glass Struct. Eng. 1 (2) (2016) 417–431.

[39] C. Bedon, C. Louter, Finite-element analysis of post-tensioned SG-laminated glass beams with mechanically anchored tendons, Glass Struct. Eng. 1 (1) (2016) 19–37, https://doi.org/10.1007/s40940-0167.

[40] M. Kozlowski, M. Kadela, J. Hulmika, Numerical investigation of structural behaviour of timber-glass composite beams, Procedia Eng. 161 (2016) 990–1000.

[41] J. Rocha, E. Pereira, J. Sena-Cruz, Alternative approaches for the numerical simulation of glass structural beams reinforced with GFRP laminates, in: Proceedings of Challenging Glass 6, 2018. ⟨http://dx.doi.org/10.7480/cgc.6.2151⟩.

[42] P. Neto, J. Alfaiate, L. Valarinho, J.R. Correia, F.A. Branco, J. Vinagre, Glass beams reinforced with GFRP laminates: experimental tests and numerical modelling using a discrete strong discontinuity approach, Eng. Struct. 99 (2015) 253–263.

[43] C. Bedon, C. Louter, Numerical analysis of glass-FRP post-tensioned beams - review and assessment, Compos. Struct. (2017), https://doi.org/10.1016/j.compstruct.2017.06.040.

[44] P. Del Linz, P.A. Hooper, H. Arora, Y. Wang, S. Smith, B.R.K. Blackman, J.P. Dear, Delamination properties of laminated glass windows subject to blast loading, Int. J. Impact Eng. 105 (2017) 39–53.

[45] M. Santarsiero, C. Bedon, C. Louter, Experimental and numerical analysis of thick embedded laminated glass connections, Compos. Struct. 188 (2018) 242–256.

[46] A. Earij, G. Alfano, K. Cashell, X. Zhou, Nonlinear three-dimensional finite-element modelling of reinforced-concrete beams: computational challenges and experimental validation, Eng. Fail. Anal. 82 (2017) 92–115.

[47] M.A. Alam, S.A. Bakkar, S.A. Onik, K.N. Mustapha, Embedded connector in severe optimization of steel plate for shear strengthening of RC beam: experimental and numerical investigation, Adv. Civil. Eng. 2018 (2018), https://doi.org/10.1155/2018/4721431.

[48] C. Amadio, C. Bedon, M. Fasan, M.R. Pecce, Refined numerical modelling for the structural assessment of steel-concrete composite beam-to-column joints under seismic loads, Eng. Struct. (2017) (138-394-409).

[49] C. Louter, J.H. Nielsen. Numerical analysis of the effect of SG-interlayer shear stiffness on the structural performance of reinforced glass beams, in: Proceedings of COST Action TU0905, Mid-term Conference on Structural Glass, 2013, pp. 405–411, ISBN 978-1-138-00044-5.

[50] S. Casolo, V. Diana, Modelling laminated glass beam failure via stochastic rigid body-spring model and bond-based peridynamics, Eng. Fract. Mech. 190 (2018) 331–346.

[51] X. Zhang, H. Hao, G. Ma, Parametric study of laminated glass window response to blast loads, Eng. Struct. 56 (2013) 1707–1717.

[52] M. Larcher, M. Arrigoni, C. Bedon, A. van Doormaal, C. Haberacker, G. Husken, O. Millon, A. Saarenheimo, G. Solomos, L. Thamie, G. Valsamos, A. Williams, A. Stolz, Design of blast-loaded glazing windows and facades: a review of essential requirements towards standardization, Adv. Civil. Eng. 2016 (2016), https://doi.org/10.1155/2016/2604232.